

Light tracking for glaciers and oceans – Scattering and absorption in heterogeneous media with PHOTONICS

J. Lundberg^{a,*}, P. Miočinović^b, T. Burgess^c, J. Adams^d,
S. Hundertmark^c, P. Desiati^e, K. Woschnagg^f, P. Niessen^g,

^a*Division of High Energy Physics, Uppsala University, Uppsala, SE*

^b*Department of Physics and Astronomy, University of Hawaii, Manoa, US*

^c*Department of Physics, Stockholm University, Stockholm, SE*

^d*Department of Physics and Astronomy, University of Canterbury, Christchurch, NZ*

^e*Department of Physics, University of Wisconsin, Madison, Wisconsin, US*

^f*Department of Physics, University of California, Berkeley, California, US*

^g*Bartol Research Institute, University of Delaware, Newark, Delaware, US*

Abstract

In the field of neutrino astronomy, glacial ice or deep ocean water are used as detector medium. Elementary particle interactions are studied using in situ detectors recording time distributions and fluxes of the faint photon fields of Cherenkov radiation, typically generated by ultra-relativistic muons.

The PHOTONICS software package was developed to determine photon flux and time distributions throughout a volume through Monte Carlo simulation. Photons are propagated and time distributions are recorded throughout a cellular grid constituting the simulation volume, and the Mie scattering is realized using wavelength and position dependent parameterisations. The photon tracking results are stored for transparent access through ANSI-C and C++ interfaces.

In this paper the PHOTONICS light propagation routines and methodology are introduced and applied to the IceCube and ANTARES neutrino telescopes. The way in which inhomogeneities of the Antarctic glacial ice distort the signatures of elementary particle interactions, and how PHOTONICS can be used to account for these effects, is described.

Key words: Numerical simulation; optical properties; Monte Carlo method; ray tracing, optical; neutrino detection.

PACS: 78.20.Bh, 02.70.Uu, 42.15.Dp, 91.50.Yf, 92.40.-t, 93.30.Ca, 95.85.Ry

1 Introduction

In optical high energy neutrino astronomy light from particle physics events is observed using a large number of detectors placed in glacial ice or deep ocean water. Successful simulation and reconstruction of such events relies on accurate knowledge of light propagation within the detector medium. Light propagating through even the clearest water or ice is affected by scattering and absorption. For light sources and receivers separated by distances comparable to the photon mean free path, scattering effects can neither be ignored nor analytically calculated. The typical scattering lengths in these detection media are of the order of tens to hundreds of metres. Since this scale is comparable to the typical detector separation, detailed simulation of the photon propagation is required to obtain information necessary for event simulation and reconstruction. The problem is complicated further by the anisotropy of the light emitted in particle interactions and the heterogeneity of detector media. PHOTONICS is a software package containing routines for detailed photon Monte Carlo simulations, which take into account such complexities to provide, in tabulated form, the photon flux distribution for an input light source throughout a specified medium. The program is freely available[1].

In this paper we first introduce the relevant physics of the photon propagation (section 2) and the details of the PHOTONICS implementation (section 3). We then compare our results with observations of calibration light sources in sea water and glacial ice (section 4). In section 5, we present some photon tracking results relevant to the detection of neutrinos with the IceCube neutrino telescope.

2 Light propagation in diffuse media

Our goal was to model the transport of light through glacial ice and water. Photon propagation depends on the optical properties of the medium, in particular on the velocity of light and the absorption and scattering cross-sections. Glacial ice is optically inhomogeneous due to depth dependent variations in temperature, pressure, and concentrations of insoluble dust and air bubbles. Since the dust deposits track climatological changes and are therefore assumed

* Corresponding author

Division of High Energy Physics, Uppsala University, Box 535

Phone: +4670-7422777

Fax: +4618 471 3513

Email address: `johan.lundberg@ts1.uu.se` (J. Lundberg).

URL: `photonics.ts1.uu.se` (J. Lundberg).

to be arranged in horizontal layers, their effect is parameterized as a vertical variation of the optical properties. In addition to this spatial variation, the wavelength dependence of the medium parameters must be taken into account. Our goal was then to model the transport of light through transparent media with wavelength and depth dependent optical properties. Before describing our implementation to achieve this goal, we review in more detail the optical quantities that must be considered in the simulation.

The time of light travel is determined by the group velocity of light, which is parameterized by the group refractive index $n_g(\lambda)$, while various transmission and scattering coefficients depend on the phase velocity [2] and its index of refraction $n_p(\lambda)$.

Absorption of visible and near UV photons in pure water and ice is due to electronic and molecular excitation processes and is characterized by the *absorption length* $\lambda_a(\lambda)$. Measurements of light attenuation in sea water have been performed at relevant wavelengths by the DUMAND, NESTOR, Baikal and ANTARES collaborations [3,4,5,6]. The AMANDA collaboration has developed an empirical model for optical absorption in deep glacial ice by combining laboratory and in situ measurements [7,8,9]. At wavelengths $\lambda < 210$ nm and $\lambda > 500$ nm, absorption is dominated by the properties of pure ice, while in the intermediate range absorption by impurities dominates.

Photon scattering by scattering centres of general sizes is described by Mie scattering theory [10], which for any wavelength and scattering centre size gives the scattering angle distribution, the *phase function*. In water and ice, light is scattered by centres of very different types and sizes: from ice crystal point defects to air bubbles and ash particles in ice, to biological matter in water. Rayleigh scattering, where the scattering centre is affected by the scattered photon, and Brillouin scattering, where photons are scattered on (thermal) density fluctuations, also occur and may result in a change of photon energy. However, these processes are subdominant to Mie scattering on air bubbles and insoluble particles (such as salt grains and mineral grains) in ice [8], and biological particles in water [6].

In natural ice and water it can be difficult to determine the phase function from in situ measurements. Instead, the IceCube and ANTARES collaborations have used calibration light sources to determine the propagation characteristics assuming certain forms of the scattering angle distributions. In the case of ice, a one parameter Henyey-Greenstein (HG) phase function is often used, approximating Mie scattering under the assumption that scattering is forward peaked [11]. For water, a two parameter phase function is more useful. For this

paper we will mostly use the single parameter HG phase function

$$\frac{dp(\cos \theta; \lambda)}{d(\cos \theta)} = \frac{1 - \tau(\lambda)^2}{2(1 + \tau(\lambda)^2 - 2\tau(\lambda) \cos \theta)^{\frac{3}{2}}}, \quad (1)$$

which is completely characterized by the $\tau(\lambda)$ parameter, the mean of the cosine of the scattering angle θ for the wavelength λ ,

$$\tau(\lambda) = \langle \cos \theta \rangle(\lambda) = \int d(\cos \theta) \cos \theta \frac{dp(\cos \theta; \lambda)}{d(\cos \theta)}. \quad (2)$$

The *absorption length*, λ_a , and *scattering length*, λ_s , are the mean free paths of exponential distributions. The probability distribution of the path length l to the next scatter is

$$\frac{dp(l; \lambda)}{dl} = \frac{e^{-l/\lambda_s}}{\lambda_s}. \quad (3)$$

When determining ice or water optical properties, there is a strong degeneracy between λ_s and τ . One therefore considers the *effective scattering length*, λ_e , defined as

$$\lambda_e = \frac{\lambda_s}{1 - \tau}. \quad (4)$$

For a collimated beam in a non-absorbing medium, λ_e has a natural interpretation as the distance in the original direction after which the net flux in that direction is zero. The projection of the photon velocity vector on its original direction is decreased on average by $\tau = \langle \cos \theta \rangle$ in each scattering step [12]. Hence, the net flux in the original direction will be zero at a forward distance of

$$\lambda_s \sum_{i=0}^{\infty} \tau^i \rightarrow \frac{\lambda_s}{1 - \tau} = \lambda_e. \quad (5)$$

3 Monte Carlo simulation implementation

In this section we present the main ingredients in our photon Monte Carlo simulation implementation. The end product is a *set* of photon flux density tables. For a given source, a user-specified large number of photons are generated according to the source characteristics and are then tracked and recorded throughout the simulation volume with the resulting photon flux tabulated in

a six dimensional table. Four of these dimensions are for the spatial and temporal location in the simulation volume with respect to the emission point. As the light sensors are assumed to have azimuthal symmetry the photon impact direction is characterized only by the zenith angle. The sixth dimension is the angle from the light source major axis at which a photon is emitted. These latter two dimensions are usually integrated over when the photon tables are used with detector simulations. For each light source position and orientation one table is produced, while a *set* of tables describes a range of source locations and directions.

3.1 Media and light source properties

As discussed in section 2, the properties of the optical medium are described by the group and phase refractive indices, n_g, n_p , the average scattering angle τ , the effective scattering length λ_e , and the absorption length λ_a . These parameters are taken to be functions of wavelength and a spatial dimension Z , typically specifying the ice or water depth. Thus, the propagation medium is divided into horizontal regions which differ by their optical properties. For media where the single parameter HG approximation does not provide an adequate description of the scattering it can be replaced by other scattering phase functions. An example of this is the treatment of sea water in section 4.1.

A single simulation run begins with the injection of a photon with wavelength and emission direction chosen from user-specified probability distributions and at a user-specified location. Our procedures support point-like (infinitesimal) light sources, where all emitted photons originate from the same point, and volume light sources where the emission is distributed over a volume. All light sources are assumed to have an axis around which the source displays mirror symmetry. An example light source, essential for neutrino astrophysics, is that of a Cherenkov emitter. In PHOTONICS a Cherenkov emitter is a point-like (infinitesimal) light source with a Cherenkov spectrum and an angular emission in a Cherenkov cone[13]. In this case the emission is symmetric about the principal axis of the Cherenkov emitter. Closely related are light sources composed of many short Cherenkov tracks, such as electromagnetic cascades. Simulation results using Cherenkov properties are presented in Section 5. Another category of sources are laser or LED light sources, and in Section 4 we compare our simulation of these sources with observations. Continuous and extended light sources are composed by integration of infinitesimal, point-like sources. For example, the light distribution due to relativistic muons are composed by integrating a series of infinitesimal Cherenkov emitters over space and time as will be described in section 3.4.

3.2 Coordinate systems for photon flux recording

The Cherenkov light source example possesses a cylindrical symmetry. Although that symmetry is typically broken by the response functions of the propagation medium and the detector, it is usually a natural choice for recording the light flux in Monte Carlo simulation, and is therefore used in the following. In addition to cylindrical (ρ, l, ϕ) coordinates, we have also included functionality to allow the flux to be recorded in spherical (r, ϑ, ϕ) or Cartesian (x, y, z) coordinates. A grid over the spatial coordinates defines cells in which the photon flux density and time distributions are averaged. In some dimensions it can be desirable to have denser binning close to the origin. Therefore, equidistant as well as linearly increasing bin size is supported for ρ, l and the time parameter t . In addition to specifying the spatial coordinates where the light flux is recorded relative to the source, the location of the source and its direction of the axis of symmetry with respect to the medium are needed. These can be characterized using just two coordinates, the depth Z_s and zenith angle Θ_s . This is due to the horizontal symmetry of the medium, as discussed in section 3.1. Figure 1 shows the coordinates and the unit cell over which the flux is recorded.

To illustrate the size of the simulation output, a binning example is shown in Table .1 for the cylindrical coordinate system. As each single precision floating point number requires four bytes, the size of this example table would be 3 megabytes. To get the total table set size this must be multiplied with the number of light source positions Z_s and zenith angles Θ_s of interest. For example, with 50 depth bins and 20 angular bins, the total *table set* size is 3 gigabytes.

3.3 Photon propagation

The photon trajectories are determined by directly performing the stochastic scattering processes, usually using the HG phase function given in equation (1). The length of each step is an exponential random variable, characterized by the local scattering length. The scattering and absorption parameters are updated, from (λ_s, λ_a) to (λ'_s, λ'_a) , when photons enter new medium regions. When this occurs, the remaining distance d' to the next scatter is given by $d' = d\lambda'_s/\lambda_s$, where d would have been the remaining distance to the next scattering centre in the former medium with scattering length λ_s .

Photon absorption is taken into account by successively updating the photon survival probability weight w as the photons propagate through regions of different absorption. For a photon tracked n steps, each considered to be within

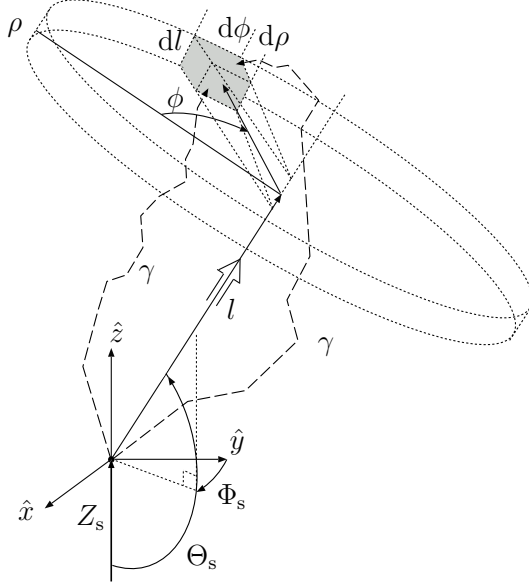


Figure 1. The unit cell geometry and photon trajectories with variables which are used for the binning of photon flux data. Photons are emitted from the light source and their flux and time distributions sampled and averaged over each spatial cell. The azimuthal direction Φ_s of the light source is degenerate since the medium is assumed to be symmetric around the \hat{z} axis.

a locally homogeneous medium, the weight is given by

$$w = \prod_{i=0}^n \exp\left(-\frac{l_i}{\lambda_a(\lambda; i)}\right), \quad (6)$$

where λ is the wavelength of the photon and l_i is the length of step i , in a region with absorption length $\lambda_a(\lambda; i)$.

The photon flux Φ (particles per area and time) at any point (ρ, l, ϕ) at a time T after the emission from a light source at a depth Z_s pointing in a direction Θ_s is denoted $\Phi(Z_s, \Theta_s, \rho, l, \phi, T - t_0(\rho, l))$, where t_0 is a reference time typically chosen to be the first time causally connected to the light emitted by the source,

$$t_0(\rho, l) = \frac{n_{\text{ref}} \sqrt{\rho^2 + l^2}}{c}, \quad (7)$$

where c is the speed of light in vacuum and n_{ref} is a user specified reference refractive index.¹ The *residual time* $t = T - t_0$ is the time delay caused by

¹ The reference time convention of Eq. (7) is suitable for point-like stationary light sources only. For fast traveling light sources such as muons a slightly different expression is used.

scattering, relative to the propagation time for a photon traveling in a straight line.

The probability density function, f_{pdf} , for a photon flux at time t is given by

$$f_{\text{pdf}}(Z_s, \Theta_s, \rho, l, \phi, t) = \frac{\Phi(Z_s, \Theta_s, \rho, l, \phi, t)}{I(Z_s, \Theta_s, \rho, l, \phi)}, \quad (8)$$

where I is the time integrated photon flux, or intensity,

$$I(Z_s, \Theta_s, \rho, l, \phi) = \int_{-\infty}^{\infty} \Phi(Z_s, \Theta_s, \rho, l, \phi, t) dt. \quad (9)$$

Since the photon fluxes are additive we can determine the time distribution of a combination of light sources through

$$f_{\text{pdf}}(t) = \frac{\sum_i I_i f_i(t)}{\sum_i I_i} = \frac{\sum_i \Phi_i(t)}{\sum_i I_i}. \quad (10)$$

The photon flux in a particular spatial cell can be calculated by one of two methods: the area-crossing method or the volume-density method. In the area-crossing method, the contribution of each photon to the total flux depends on the projected surface area of a unit cell as seen from the direction of the photon at the time the photon crosses the cell boundary. In the volume-density method, all photons that enter a unit cell contribute to its photon density, which is converted to the total flux through multiplication with the distance Δs between photon position sampling points. The respective equations for the calculation of flux per emitted photon are

$$\Phi_{\text{AreaCrossing}} = \frac{1}{N} \sum_{\gamma} w_{\gamma} A_{\perp}^{-1} = \sum_{\gamma} w_{\gamma} \left(\sum_S \hat{\mathbf{d}}_{\gamma} \cdot \vec{\mathbf{A}}_S \right)^{-1}, \quad (11)$$

$$\Phi_{\text{VolumeDensity}} = \frac{1}{N} \sum_{\gamma} w_{\gamma} \frac{\Delta s}{V}, \quad (12)$$

where the γ sum runs over the N simulated photons, w_{γ} is the survival weight of each photon, A_{\perp} is the unit cell area projected perpendicular to the direction of the photon, V is the volume of the unit cell and Δs is the step size used for photon tracking. The S sum runs over unit cell surfaces with areas A_S which are projected onto the photon direction $\hat{\mathbf{d}}_{\gamma}$.

The calculation and recording of a photon's contribution to the flux in a unit cell is the most expensive computational step, thus a suitable choice of calculation method (area crossing or volume-density) can speed up the simulation.

To optimize for speed and accuracy one considers the parameter $\Delta s/D_{\text{uc}}$, the ratio of the step size to the scale dimension of a unit cell. If $\Delta s/D_{\text{uc}} < 1$, the area-crossing method is efficient; otherwise, the volume-density method should be used. Thus, the area-crossing method typically results in a faster code execution for large detection volumes with large unit cells, while the volume-density method is faster for small, dense unit cell configurations.

Another way to improve the speed of the Monte Carlo simulation is through importance-weighted scattering. This means that the photons are propagated using scattering parameters which are different from those of the scattering problem to be solved in order to get better statistics at low probability phase space locations. When solving a Monte Carlo problem for random numbers x_i (for example, scattering angles) from a probability density distribution $f_1(x)$, we can choose to instead sample from another distribution $f_2(x)$ while applying a weight of $f_1(x_i)/f_2(x_i)$. As an example, photons can be propagated using isotropic scattering while weighting with the physical scattering distribution. For the Henyey-Greenstein function, the τ parameter can be modified so as to correspond to an effective scattering length a factor k_τ longer than that of the physical medium to be simulated. Equation (4) implies $\tau_2 = (k_\tau - 1 - \tau_1)/k_\tau$. For importance sampling of the scattering lengths λ_s , the f_2 distribution is taken to be an exponential distribution scaled with another factor k_s . Selecting $k_s > 1$ and $k_\tau > 1$ oversamples straighter paths and can be useful for enhancing the statistics of early photons at large source–receiver distances.

We have described how the photon flux density is calculated in cells throughout the simulation volume. In neutrino astronomy, the quantity of interest is the number of photons detected by an optical detector such as a photomultiplier (PM). As the PM response is wavelength and angle dependent, and as we do not want to store the wavelength and arrival direction of the simulated photons, it is practical to be able to fold the PM response into our simulation. Wavelength and angular efficiency files are used to weight the photon flux density to obtain the detected photon flux. Fresnel transmittance and absorbance by detector components can also be included.

3.4 *Propagating light sources*

To this point we have discussed how to obtain a set of tables describing the photon flux from a point-like, stationary light source for a range of locations and orientations. A propagating light source is different in that it can not be satisfactorily approximated as a flash of light from a single spatial point. We frame the following discussion of modeling propagating sources using high energy muons, which give rise to kilometer scale Cherenkov emitting tracks in water or ice. Our method, however, applies also to other line-like light sources

such as high energy tauons.

To calculate the photon flux distribution generated by a muon we integrate over the photon flux distributions of many point-like Cherenkov emitters. A set of point-like photon tables provide the differential light flux at any space-time location from sources at any causally connected location. This serves as integration kernel, $\Phi_{\text{point}}(\mathbf{x}_s, t_s, \mathbf{x}_{\text{rec}}, t_{\text{rec}})$, where \mathbf{x}_s, t_s and $\mathbf{x}_{\text{rec}}, t_{\text{rec}}$ are the emission and receiver coordinates for calculating the propagating source light distribution. For now, we will omit the explicit dependency on Θ_s since the symmetry axis is fixed for a light source traveling in a straight line. The integrated flux distributions are generated by convolving this kernel with a delta function propagating through space along the track of the muon. To ensure numerical stability we use linear interpolation in all dimensions (not shown) and operate on integrals (cumulative sums),

$$\Phi_{\mu}(\mathbf{x}_{\text{rec}}, t_{\text{rec}}) = \frac{d}{dt_{\text{rec}}} \int_{t_{\text{smin}}}^{t_{\text{smax}}} dt_s \int_{-\infty}^{t_{\text{rec}}} dt' \Phi_{\text{point}}(\mathbf{x}_s(t_s), t_s, \mathbf{x}_{\text{rec}}, t'). \quad (13)$$

The resulting light flux is stored in tables just as those of the point-like light sources. In principle, this integration can also be done by the detector Monte Carlo or event reconstruction codes, but such an approach would be significantly slower since the number of considered events, and therefore the number of required flux calculations, is typically large.

The integral over the source path need not necessarily be taken from or to infinity. Most often, the user would need to consider tracks of varying lengths. To provide photon flux for any given track length, without having to dynamically perform the time consuming integration of Eq. (13), we have developed a scheme based on the subtraction of semi-infinite tracks. A semi-infinite track is a track with a defined starting or stopping point, and with sufficient length such that away from this point, the recorded flux approach that of a truly infinite track. The flux at $(\mathbf{x}_{\text{rec}}, t_{\text{rec}})$ arising from a finite muon starting at \mathbf{x}_A and stopping at \mathbf{x}_B can be expressed as the difference between two such semi-infinite tracks. For two semi-infinite starting tracks, one (denoted $A \rightarrow$) starting at the point \mathbf{x}_A and another ($B \rightarrow$) starting at \mathbf{x}_B located further along the muon track, we write

$$\Phi_{\mu_{AB}}(\mathbf{x}_{\text{rec}}, t_{\text{rec}}; \mathbf{x}_A, \mathbf{x}_B) = \Phi_{\mu_{A \rightarrow}}(\mathbf{x}_{\text{rec}}, t_{\text{rec}}; \mathbf{x}_A) - \Phi_{\mu_{B \rightarrow}}(\mathbf{x}_{\text{rec}}, t_{\text{rec}}; \mathbf{x}_B). \quad (14)$$

This principle is depicted in figure 2 (I.–III.). The finite track pdf, as per Eq. (10) is given by

$$f_{\mu_{AB}}(\mathbf{x}_{\text{rec}}, t_{\text{rec}}; \mathbf{x}_A, \mathbf{x}_B) = \frac{\Phi_{\mu_{A \rightarrow}}(\mathbf{x}_{\text{rec}}, t_{\text{rec}}; \mathbf{x}_A) - \Phi_{\mu_{B \rightarrow}}(\mathbf{x}_{\text{rec}}, t_{\text{rec}}; \mathbf{x}_B)}{I_{\mu_{A \rightarrow}}(\mathbf{x}_{\text{rec}}; \mathbf{x}_A) - I_{\mu_{B \rightarrow}}(\mathbf{x}_{\text{rec}}; \mathbf{x}_B)}. \quad (15)$$

Alternatively, we can use two semi-infinite stopping tracks, stopping at the same points \mathbf{x}_A and \mathbf{x}_B , and write

$$\Phi_{\mu_{AB}}(\mathbf{x}_{\text{rec}}, t_{\text{rec}}; \mathbf{x}_A, \mathbf{x}_B) = \Phi_{\mu \rightarrow B}(\mathbf{x}_{\text{rec}}, t_{\text{rec}}; \mathbf{x}_B) - \Phi_{\mu \rightarrow A}(\mathbf{x}_{\text{rec}}, t_{\text{rec}}; \mathbf{x}_A), \quad (16)$$

$$f_{\mu_{AB}}(\mathbf{x}_{\text{rec}}, t_{\text{rec}}; \mathbf{x}_A, \mathbf{x}_B) = \frac{\Phi_{\mu \rightarrow B}(\mathbf{x}_{\text{rec}}, t_{\text{rec}}; \mathbf{x}_B) - \Phi_{\mu \rightarrow A}(\mathbf{x}_{\text{rec}}, t_{\text{rec}}; \mathbf{x}_A)}{I_{\mu \rightarrow B}(\mathbf{x}_{\text{rec}}; \mathbf{x}_B) - I_{\mu \rightarrow A}(\mathbf{x}_{\text{rec}}; \mathbf{x}_A)}. \quad (17)$$

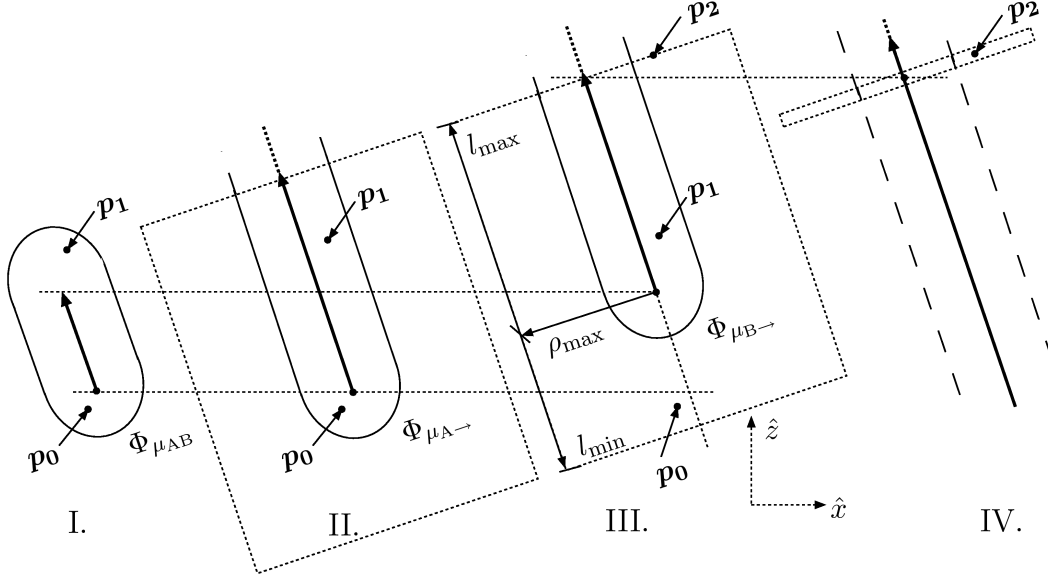


Figure 2. Finite track constructed by subtraction of two semi-infinite tracks, as explained in the text. The light distribution (in time and space) of the finite track (I.) is the difference between the two semi-infinite tracks (II.) and (III.). The dotted rectangles show the outer limits of the tabulated semi-infinite tables. The rightmost figure (IV.) represents the special infinite track tables with just one l bin per table. The representation of photon flux at a point \mathbf{p}_2 far from the starting and stopping points, can be done in two ways. Either, as in (III.), by considering the edge of a semi-infinite table, or as in (IV.) with an *infinite* track table with only a single l bin, that is, $l = 0$.

Mathematically, using either starting or stopping semi-infinite track information is sufficient for describing any finite track anywhere within the simulated volume. However, it is numerically superior to dynamically choose between both these descriptions depending on where on the finite track a query is being made. As an example, consider the point \mathbf{p}_0 , close to the finite track start point. The photon distribution at this point is best described as the difference between two semi-infinite starting tracks (Eq. 14), since $\Phi_{\mu_{B \rightarrow}}$ is small and $\Phi_{\mu_{AB}} \approx \Phi_{\mu_{A \rightarrow}}$. However, at the point \mathbf{p}_1 closer to the end of the finite track, $\Phi_{\mu_{A \rightarrow}} \approx \Phi_{\mu_{B \rightarrow}}$ so that the calculation of $\Phi_{\mu_{AB}}$ becomes dependent on exact numerical cancelation. In this case, using semi-infinite stopping tracks (Eq. 16) would be superior. Our algorithms chooses dynamically between Eq. (14) and Eq. (16) based on which of the vertices is closer to the observation point. It

allows dynamic and fast access to the finite track photon distribution without the need for real time integration.

In some cases, it is sufficient to consider a track as semi-infinite, either starting or stopping depending on which of the subtracted quantities in Eq. (14–17) can be neglected. In the intermediate region, any of the descriptions are valid.

It can even be desirable to regard tracks as completely infinite. By using the degeneracy of infinite tracks with respect to a starting/stopping point, such tables can be made much smaller, since there is one dimension less to consider, namely l . For each l , one can find another source location z , with a different l , corresponding to exactly the same light profile. Figure 2 (III. and IV.) illustrates the two ways of accessing information about virtually infinite tracks. In Figure 2(IV.), a special, degenerate, *infinite* table with a single l bin ($l = 0$) is shown. The size of an infinite table is typically about 1% of the size of the corresponding semi-infinite description, which can be on the order of tens of gigabytes. Hence, the infinite tables can easily be loaded into computer memory all at once, which is particularly useful in event reconstruction, where it can be hard to estimate in advance the properties of an event to be reconstructed. Since only redundant information is removed, the degenerate muon tables contain exactly the same level of flux details, under the infinite track assumption. Reconstruction and large table support is discussed in the following section, describing the PHOTONICS reader library.

3.5 Accessing photon flux simulation results

We provide a convenient interface to the PHOTONICS flux tables for incorporating the photon flux results into experiment simulation or event reconstruction. Its functionality can be accessed directly using a set of ANSI-C functions and procedures, or through a more abstract (ROOT compliant) user interface written in C++. A simulation chain for a whole experimental setup can be achieved by using these interfaces in combination with routines applying detector specific details such as modeling of the electronics and data acquisition. For event reconstruction, PHOTONICS provides probability density functions (pdf) for individual photons, and the expected number of detected photons N , which is based on a photon flux intensity. These can be used by track-fitting algorithms, for example maximum-likelihood routines.

Using the table reader library, the user can query the photon flux tables by specifying location, orientation and other properties of sources, as well as the location of the light detectors. On request, a set of tables are loaded into memory, and the reader library determines which of the loaded tables best matches the user request. PHOTONICS performs linear interpolation in

all dimensions (individually enabled using a bitmask) for time integrated flux and pdf values.

Any number of table sets can be loaded simultaneously (limited only by available memory), making it possible to simulate or reconstruct the cumulative signal from different types of light sources. This is useful, for example, in the simulation of secondary electromagnetic showers from a primary muon track. In an experiment simulation, the user first requests the expected number of detected photons, specifying light source and detector positions, $N(\mathbf{x}_{\text{rec}}, \mathbf{x}_s, \Theta_s, E, L)$, where \mathbf{x}_s and \mathbf{x}_{rec} are the light source and receiver locations, L is the light source length if applicable (as described in section 3.4), and E is the light source energy used for scaling the light source intensity. The expected photon number query also returns a photon flux table reference which can be used to get photon arrival times randomly drawn from the tabulated time distribution at the corresponding coordinates. For event reconstruction, the pdf is provided in the form $f_{\text{pdf}}(\mathbf{x}_{\text{rec}}, \mathbf{x}_s, \Theta_s, t, L)$. Both photon intensity and f_{pdf} are naturally continuous in L and E , and are made continuous in $\mathbf{x}_{\text{rec}}, \mathbf{x}_s, \Theta_s, t$ by multidimensional linear interpolation. The interpolation of time distributions is flux weighted, in agreement with (10),

$$f_{\text{pdf}} = \frac{\sum_i w_i I_i f_i}{\sum_i w_i I_i}, \text{ with } \sum_i w_i = 1. \quad (18)$$

In event reconstruction, it can also be desirable to convolve the differential time distributions with the detector time response function or the emission time distribution. This can be done using a routine operating on the simulated photon flux tables. As examples, we have implemented Gaussian convolution as well as two light source time distributions described in [6] (see section 4).

Since detailed photon table sets are often many times larger than the primary memory of a computer, we provide some memory management tools. Users can dynamically load and unload tables, and select loading of tables corresponding to limited ranges of depths (Z_s) and light source angles (Θ_s). In experiment simulations, this is particularly useful, since the parameters of a particle to be simulated can be known beforehand. In event reconstructions, the fitting algorithms need to be restricted to the interval covered by the loaded tables. The regions of interest can first be determined with a set of smaller PHOTONICS tables (for muons, this could be the much smaller *infinite* tables, see section 3.4) or by using other first-guess approaches.

In addition to what has already been mentioned, the PHOTONICS package includes several other tools for processing of the photon flux tables, including integration in any dimension and conversion between differential and cumulative time distributions.

4 Comparison with observations

In this section we use measurements with artificial calibration light sources in deep sea and glacial ice to demonstrate that PHOTONICS accurately reproduces the general behavior of the observed photon distributions.

4.1 *Modeling of natural water and ANTARES' Mediterranean water surveys*

The ANTARES collaboration is constructing a 0.1 km^2 water neutrino detector in the deep Mediterranean sea [6]. In the present design the detector has 12 vertical strings, each of which has a total height of about 350 metres and consist of 25 storeys made up of three optical modules.

Three strings were deployed in 2006 and the remaining strings are scheduled to be installed during 2007.

Absorption and effective scattering lengths in the deep Mediterranean sea water have been investigated by the ANTARES collaboration and presented in Ref. [6]. The surveys were performed during several seasons using a calibrated setup of isotropic light sources, one in the blue at 473 nm, and one in UV at 375 nm. For blue (UV) they quote λ_a of 60 (26) m and λ_e of 265 (122) m, with 15% time variability. The details of the experimental setup such as the time distributions of the light emission from the source and detector efficiency curves, play a large role in the details of the photon flux time distribution profile in media, like ocean water, where scattering is weaker than absorption. In addition, since the light will typically be observed at distances smaller than or comparable to the effective scattering length, the scattering phase function plays an even larger role. ANTARES assumed a weighted sum of a Petzold and a molecular (Einstein-Smoluchowski) distribution. The Petzold distribution has $\tau=0.924$, and is here approximated by a HG distribution, while the molecular distribution is approximated by a second HG distribution with $\tau=0$. Figure 3 compares our simulation results using this model, for distances of 24 and 44 m from the light source, with ANTARES measured distributions of June 2000 [6]. The agreement verifies the validity of the model given in [6] and our photon flux simulation for this case.

4.2 *Modeling of ice and ICECUBE's Antarctic glacial ice surveys*

The IceCube neutrino telescope, under construction deep in the Antarctic glacial ice, is planned to become a high-energy neutrino detector of roughly 1 km^3 instrumented volume[14]. It is planned to have 80 strings, of which 22 have

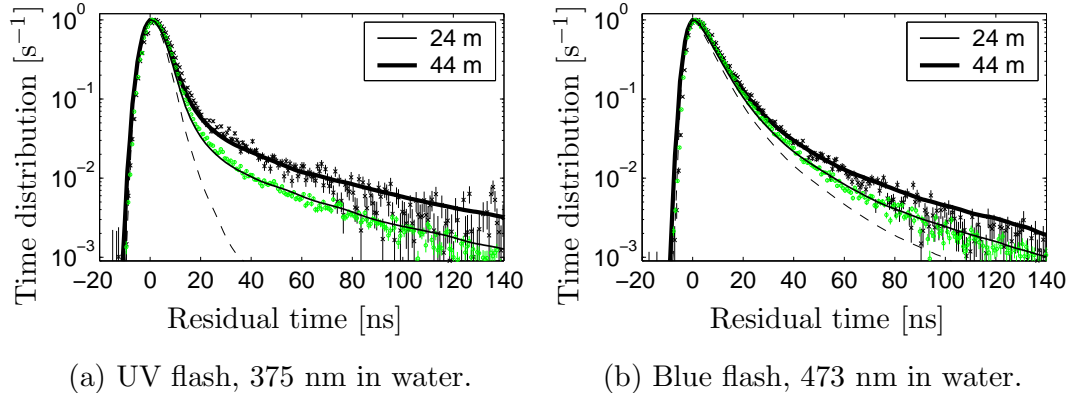


Figure 3. Simulated time distributions at distances 24 m (thick line) and 44 m (thin line) from monochromatic flashes in water. The circles and stars show calibration data from the ANTARES collaboration, while the lines show our simulation results. The time distributions of the light sources (dashed lines) were measured in air, where scattering and absorption can be neglected. We use the water properties and experimental data of ref [6] and apply the same convention to normalize the time distributions to the peak value.

been deployed so far, each equipped with 60 encapsulated PMs distributed over the depth of a kilometre. It builds on to the 19 strings of the AMANDA array.

A detailed study of the properties of the deep Antarctic glacial ice has been performed by the AMANDA collaboration. All model parameters used in this section were determined in the work presented in [9]. The glacial ice is very clear in the optical and near UV with absorption lengths of 20–120 m depending on wavelength. The effective scattering lengths are on the order of 25 m, less for shorter wavelengths. Both scattering and absorption are strongly depth dependent and vary on all depth scales. The variations at depth greater than 1450 m, where bubbles no longer exist, are explained by changes in climatic conditions which correlate with concentrations of insoluble dust deposits. By using physics motivated functional forms for the wavelength and depth dependencies of scattering and absorption, the AMANDA collaboration fitted a large number of recorded light distributions generated by in situ pulsed and steady light sources at different wavelengths to form a heterogeneous ice model. At each 10 m depth interval, the effective scattering and absorptions lengths, λ_e and λ_a as function of wavelength was determined.

We have calculated the time distributions corresponding to two combinations of wavelength and light source–receiver positions, and compare them with experimental distributions. Our results are shown in figure 4. The dots show the time distributions of experimental data, while the solid lines show our simulation results. Thick black lines show our results when using the scattering and absorption parameters measured with these particular source–receiver combinations[9], with a gray shaded area representing two opposing deviations within the parameter uncertainty of these models. The parameters of the sin-

gle data point models were $\lambda_e = 27.6$ m, $\lambda_a = 20.5$ m for the 532 nm curve, and $\lambda_e = 22.6$ m, $\lambda_a = 82.0$ m for the 470 nm curve, both with $\tau = 0.94$. The slight overestimation in the tail in figure 4(b) is due to a large uncertainty in the measured absorption length for this particular case. The thin lines show our simulation results with the heterogeneous ice model which is based on data from many source–receiver combinations at different depths and wavelengths.

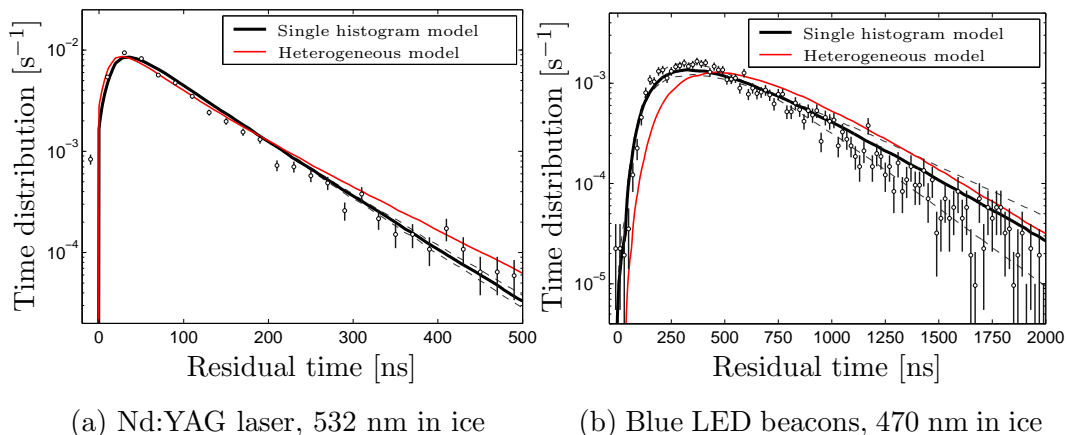


Figure 4. Residual time distributions of simulated light pulses in deep glacial ice. In (a), we show the time distribution of photons emitted from a 532 nm Nd:YAG isotropic laser pulse, emitted at a depth of 1825 meter, as seen from a horizontal distance of 75 m. In (b), we show the time distributions, at a horizontal distance of 140 m, from an upward pointing 470 nm LED emitter located at a depth of 1580 m. The intrinsic timing widths of the light sources, less than 10 ns, were here ignored. The black dots show two time distributions of glacial ice surveys, with vertical Poissonian error bars. The thick black lines show our results using the scattering and absorption parameters of these particular source–receiver combinations, and thin dashed lines represent two opposite parameter variations within parameter uncertainty. The thin lines show our simulation results with the heterogeneous ice model. The ice model parameters were determined in the work presented in [9] where the data is also found.

5 Application to neutrino astronomy

In neutrino astronomy, the universe is studied using high energy neutrinos as messengers. The neutrinos are only detected after interacting with matter in the vicinity of the neutrino telescope and producing charged, Cherenkov light emitting particles like muons. Some of the emitted light is recorded by optical sensors distributed throughout the detector volume.

Ultra-relativistic muons are the primary channel through which high energy neutrinos are detected by optical neutrino telescopes. They are also the primary background in the form of so-called atmospheric muons arising from high energy cosmic-ray interactions in the Earth’s atmosphere. Since the way

of distinguishing a neutrino signal from the background is through energy spectra and angular distributions, it is important to establish the particle energy and the direction in every recorded event as accurately as possible. Our software contributes to this aim by providing means for detailed photon flux simulations, using the optical properties as established at a specific site. To further illustrate the utility of PHOTONICS, we present in this section photon propagation results for the inhomogeneous ice at the site of the IceCube neutrino telescope, using the heterogeneous ice model of [9].

The flux in all figures is given per emitted photon, and is weighted with the angular and wavelength dependent acceptance of optical detectors, so that the figures display the expectation number of detections per square meter of the detector module. It is not scaled to represent any particular light source energy.

Figure 5 shows the photon flux from an infinitesimal electromagnetic cascade. Cascades are initiated in muon energy loss processes as well as in primary neutrino interactions. The light spectra of hadronic and electromagnetic cascades are also Cherenkov in nature, but the light originates from many Cherenkov light emitting particles. Since the trajectories of the emitting particles are not necessarily parallel to the parent particle, the Cherenkov emission cone is distorted[15]. The photon flux of figure 5 is that of a simulated point-like cascade, located in the IceCube detector site ($Z_s = 0$, at a depth of 1730 m). The cascade is oriented towards the surface at $\Theta_s = 135^\circ$, up and left in the figures. A vertical slice through the photon flux, containing the principal axis of the light source origin is displayed. The angular distribution of emitted photons is peaked at the Cherenkov angle, but the photon flux is smoothed out by scattering as it evolves through the ice. After 100 ns, we can still observe a peaked light distribution in the forward direction. At later times, the flux becomes more and more isotropic, to finally resemble that of an isotropic flash.

The photon flux tables used for these figures were convolved with a 10 ns Gaussian to account for PM jitter, which is useful in event reconstruction but in experiment simulation it is easy to apply the random jitter times to each photon. A strength of our simulation is that we can include angular variation in the acceptance of the detectors. Since the IceCube PMs are pointed downwards they detect up-going light with a higher efficiency than down-going light, which needs to be scattered to reach the PM photocathode. This results in the direction of a light source appearing to point higher (more upward) than it actually points. This can be seen in Figure 5 where the direction of the light source appears to be oriented at an angle larger than $\Theta_s = 135^\circ$.

While the ice is very clear in the centre of the AMANDA telescope, there are other depths where stronger scattering and absorption distort the photon flux.

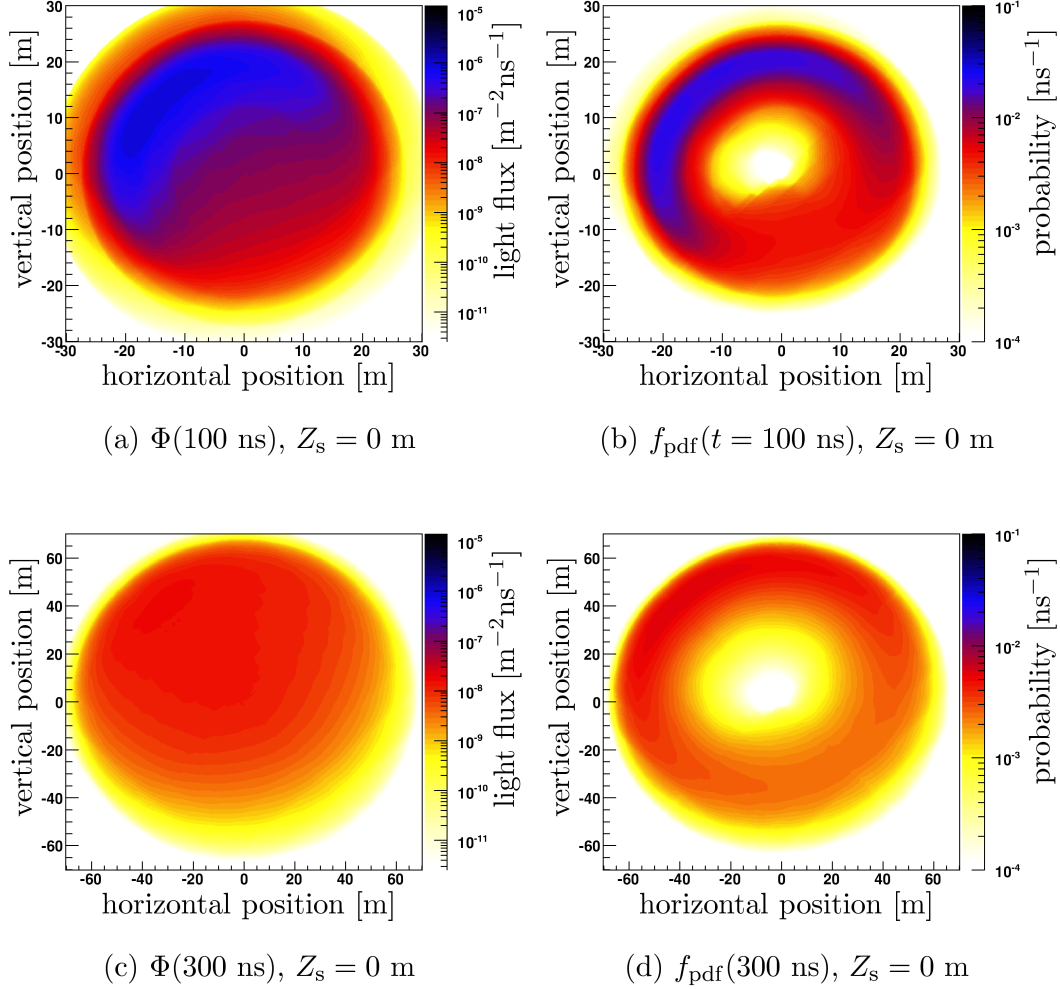


Figure 5. The ice is very clear in the centre of the AMANDA telescope. The upper panel shows a vertical slice of the photon flux, $\Phi(t)$ (a) and the probability distribution $f_{\text{pdf}}(t)$ (b) at a time $t = 100 \text{ ns}$ after light emission at the centre. The lower panels show the same distributions at $t = 300 \text{ ns}$. Note the different scales of the upper and lower panels.

In the upper panel of figure 6 results are shown for a setup analogous to that of figure 5 but with the shower origin placed 350 m deeper in the ice. This location is immediately below a region of peak scattering and absorption. The direction is the same, $\Theta_s = 135^\circ$, but due to the particular medium profile, the particle track appears more isotropic, or even downward pointing. However, it does differ from truly downward pointing events at the same location, shown in the lower panel of figure 6. In this particular case it is exceptionally hard to characterize the event correctly, but by using the correct heterogeneous medium profile we improve the possibility to distinguish these cases. This is important for event simulation and reconstruction of parameters such as the zenith angle and the cascade energy.

We now turn our focus to muons. Figure 7 shows the light distribution of a sim-

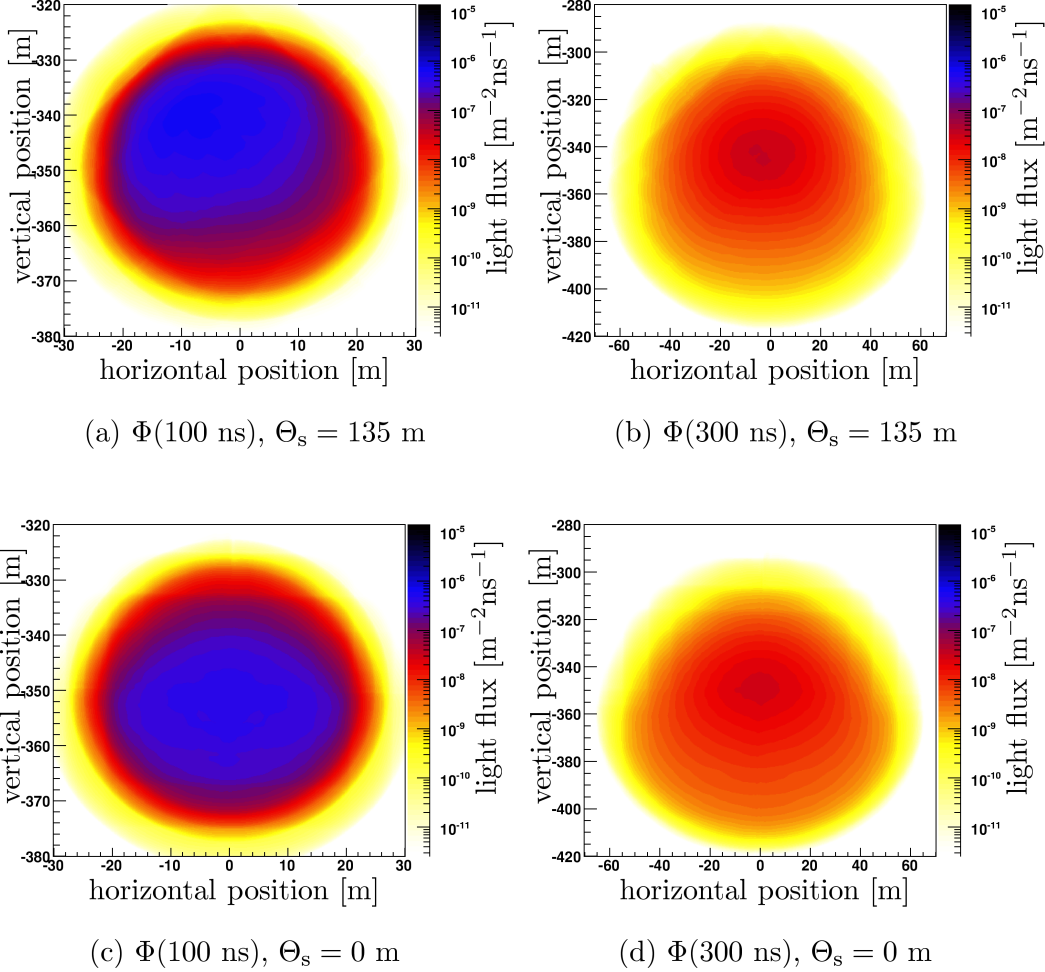


Figure 6. Regions of higher scattering and absorption distort the light distributions. All figures show the photon flux $\Phi(t)$ for a cascade positioned 350 m below the AMANDA centre. This location is immediately below a region of peak scattering and absorption. The time indicated is the time since light emission. Due to the large scattering and absorption just above the emission point, the flux of the upward pointing source evolves from a Cherenkov angle peaked distribution to a distribution which is similar to that of a downward pointing source. The upper panel, (a) and (b), can be directly compared with figure 5, which shows an identical setup, but with the source located at the AMANDA centre. The photon flux time evolution the corresponding downward pointing source is shown in the lower panel, (c) and (d).

ulated muon moving upwards, on its way through the point $x = 0, z = 0$. At the front of the track, we observe a cross section of the unscattered Cherenkov wavefront, followed by a diffuse light cloud as the photons are scattered away from the geometrical Cherenkov cone. At locations with more scattering, photons are obstructed and absorbed before they can travel very far. This deforms the conical light front, which appears to be bent backwards as is easily observed in the $f_{\text{pdf}}(t)$. We observe a weak deflection of the photons with higher flux $\Phi(t)$ both above and below the dusty region near $z = -350 \text{ m}$.

Figure 8 shows the light generated by a 141 metre long muon track. The muon was created at the origin and propagated upwards at $\Theta_s = 135^\circ$ until it decayed at $x = -100, z = 100$. The figure shows a snapshot 147 ns after the muon disappeared. The probability density function $f_{\text{pdf}}(t)$ of these rather short tracks shows a shape that is similar to point-like cascades. Using the correct medium and light source description allows us to isolate the difference in light profiles of these different cases.

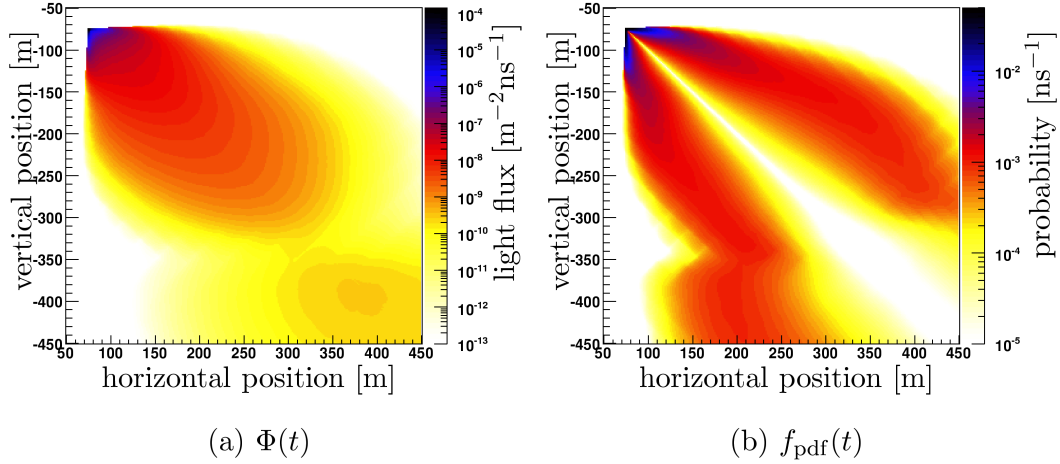


Figure 7. A snapshot of the light distribution produced by a muon which entered from below. Inhomogeneities of the medium results in a bent shape most easily seen in $f_{\text{pdf}}(t)$ (b). In (a), higher fluxes $\Phi(t)$ are observed both above and below the dusty region around $z = -350$ m.

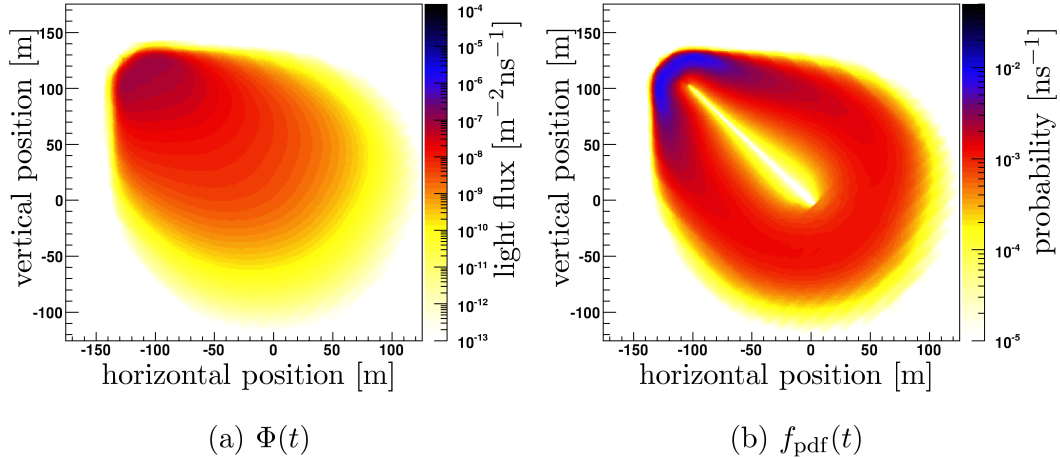


Figure 8. A 142 m long muon track in ice. This muon was created at the origin and propagated upwards at $\Theta_s = 135^\circ$ until it decayed at the $x = -100, z = 100$ point. The figures shows a snapshot 147 ns after the muon itself disappeared. (a) The photon flux $\Phi(t)$, and (b) the probability density function $f_{\text{pdf}}(t)$ which for such comparably short track shows a distribution reminiscent to one produced by point-like cascade. The light from secondary events, the cascades responsible for the muon energy loss, was not included in this simulation.

6 Conclusion

In this paper we have introduced the concepts, methods and routines which combine into the PHOTONICS software package. We have explained how the program can be used for calculating and tabulating light distributions around a stationary or moving source, as a function of time and space in scattering and absorbing heterogeneous media. The light distributions obtained from our Monte Carlo simulation agree well with observations of calibration light sources in deep sea water and glacial ice surveys. In the last section, we demonstrated how PHOTONICS can be used to model how optical inhomogeneities of the Antarctic ice at the location of the IceCube neutrino telescope distort the footprints of elementary particle interactions.

7 Acknowledgments

We are grateful to Dr. Nathalie Palanque-Delabrouille for supplying the data from the ANTARES collaboration surveys and her helpful advice in how to implement the scattering and absorption parameters derived by ANTARES into our simulation. We also thank the members of the AMANDA and IceCube collaborations for fruitful discussions and useful feedback.

References

- [1] PHOTONICS, online reference; <http://photonics.tsl.uu.se>
- [2] P. B. Price and K. Woschnagg, Role of Group and Phase Velocity in High-Energy Neutrino Observatories, *Astropart. Phys.* 15 (2001) 97
- [3] H. Blood, J.G. Learned, F. Reines, A. Roberts, *Proc. Int. Neutrino Conf., Aachen (1976)* 688; DUMAND Collaboration. *Proc. Int. Cosmic Ray Conf., 25th, Durban, S. Africa, 1997*, astro-ph/9705198
- [4] E. G. Anassontzis et al., Light transmissivity in the NESTOR site, *Nucl. Instr. and Meth.* A349 (1994) 242
- [5] I.A. Belolaptikov et al., Variation of Water Parameters at the Site of the Baikal Experiment and their Effect on the Detector Performance, *Proceedings of the 24th International Cosmic Ray Conference, Rome, Vol.1 (1995)* 770
- [6] J. A. Aguilar et al., Transmission of light in deep sea water at the site of the ANTARES neutrino telescope, *Astropart. Phys.* 23 (2005) 131
- [7] AMANDA Collaboration: P Askebjør et al., Optical Properties of deep ice at the South Pole: Absorption, *Appl. Optics* 36 (1997) 4168

- [8] P. B. Price and L. Bergström, Optical Properties of deep ice at the South Pole: Scattering, *Applied Optics* 36 (1997) 4181.
- [9] AMANDA Collaboration: M. Ackermann et al, Optical Properties of Deep Glacial Ice at the South Pole, *J. Geophys. Res.* 111 (2006) D13203
- [10] G. Mie, Beiträge zur Optik trüber Medien, speziell kolloidaler Metallösungen, *Ann. Phys.* 25 (1908) 377
- [11] L. Henyey and J. Greenstein, Diffuse radiation in the galaxy , *Astrophys. Journal*, vol. 93 (1941) 70
- [12] S. Chandrasekar. Radiative Transfer, Dover Publications, New York 1960
- [13] J. V. Jelly, Cerenkov Radiation and Its Applications, Pergamon: London (1958)
- [14] IceCube Collaboration: A. Achterberg et al, First Year Performance of the IceCube Neutrino Telescope, *Astropart. Phys.* 26 (2006) 155
- [15] C. Wiebusch, The Detection of Faint Light in Deep Underwater Neutrino Telescopes, Phd thesis, RWTH Aachen December 1995, PITHA 95/37

Tables

Dimension		Bins	Low	High
Radial	ρ	30	0 m	500 m
Longitudinal	l	51	-500 m	500 m
Azimuthal	ϕ	10	0°	180°
Time	t	50	0 ns	6000 ns

Table .1

An example of table binning using cylindrical coordinates. The rotational symmetry of the emitter and the horizontal symmetry of the medium implies an azimuthal symmetry in ϕ , so that the flux is the same at $-\phi$ and ϕ .